For a star at angular position $\boldsymbol{\alpha}$, the slope is measured in subaperture $(u,v)$, where $u$ and $v$ denote the position of the subaperture in the SH array in the horizontal ($x$) and vertical ($y$) directions. The slope, denoted $\mathbf{s}_{u,v}(\boldsymbol{\alpha})$, is a bidimensional vector with components $s_{u,v}^k$ along the $k$-axis, $k \in \{x,y\}$. The star intensity in the subaperture $(u,v)$, $i_{u,v}(\boldsymbol{\alpha})$, leads to the relative intensity fluctuation $\delta i_{u,v}(\boldsymbol{\alpha}) = \frac{i_{u,v}(\boldsymbol{\alpha}) - \langle i_{u,v}(\boldsymbol{\alpha}) \rangle}{\langle i_{u,v}(\boldsymbol{\alpha}) \rangle}$ where $\langle i_{u,v}(\boldsymbol{\alpha}) \rangle$ is the temporal average of $i_{u,v}(\boldsymbol{\alpha})$.

Spatial correlations of slopes $\langle s_{u,v}^k(\boldsymbol{\alpha}) s_{u+\delta u, v+\delta v}^l(\boldsymbol{\alpha}+\boldsymbol{\theta}) \rangle$ and spatial correlations of scintillation $\langle \delta i_{u,v}(\boldsymbol{\alpha}) \delta i_{u+\delta u, v+\delta v}(\boldsymbol{\alpha}+\boldsymbol{\theta}) \rangle$, calculated between subapertures $(u,v)$ and $(u+\delta u, v+\delta v)$, of separation vector $\boldsymbol{\rho} = (\delta u, \delta v)$, are directly related to integrals of the $C_n^2(h)$ weighted by theoretical functions $W_{ss}^{kl}$ and $W_{ii}$ and are written as:

$$\langle s_{u,v}^k(\boldsymbol{\alpha}) s_{u+\delta u, v+\delta v}^l(\boldsymbol{\alpha}+\boldsymbol{\theta}) \rangle = \int_0^{+\infty} C_n^2(h) W_{ss}^{kl}(h,\boldsymbol{\rho},\boldsymbol{\theta}) \, \mathrm{d}h, \tag{1}$$

$$\langle \delta i_{u,v}(\boldsymbol{\alpha}) \delta i_{u+\delta u, v+\delta v}(\boldsymbol{\alpha}+\boldsymbol{\theta}) \rangle = \int_0^{+\infty} C_n^2(h) W_{ii}(h,\boldsymbol{\rho},\boldsymbol{\theta}) \, \mathrm{d}h, \tag{2}$$

where $\langle \rangle$ denotes the averaging over time series. These expressions are derived from the theory of anisoplanatism effect in the weak perturbation regime [15]. $W_{ss}^{kl}$ and $W_{ii}$ are weighting functions that depend on the turbulence spectrum (which is commonly described using a von Kármán spectrum), the altitude $h$, the separation vector $\boldsymbol{\rho}$ between the subapertures, and the star separation $\boldsymbol{\theta}$.

In CO-SLIDAR, we compute both cross-correlations, combining the measurements on the two stars, and auto-correlations, corresponding to the measurements on a single star (case $\boldsymbol{\theta} = 0$ in Eqs. (1) and (2)). Correlations of slopes bring sensitivity to ground and low altitude layers, whereas correlations of scintillation mainly give sensitivity to high altitude layers.

## 2.2. Direct problem

In CO-SLIDAR, we currently only exploit correlations of $x$-slopes, of $y$-slopes and of scintillation for reason of computing time and because cross-correlations between $x$ and $y$-slopes are generally weaker. Correlations are averaged over all pairs of subapertures with given separation and represented as auto- and cross-correlation maps, with horizontal and vertical dimensions $2 \times n - 1$, where $n$ is the number of subapertures across the telescope diameter. Then, one pixel of these maps represents the pseudo-measurement that can be written, respectively for correlations of slopes and of scintillation, as:

$$C_{ss}^{kk}(\delta u, \delta v, \boldsymbol{\theta}) = \frac{\sum_{u,v} \langle s_{u,v}^k s_{u+\delta u, v+\delta v}^k \rangle (\boldsymbol{\theta})}{N(\delta u, \delta v)}, \quad k \in \{x,y\}, \tag{3}$$

$$C_{ii}(\delta u, \delta v, \boldsymbol{\theta}) = \frac{\sum_{u,v} \langle \delta i_{u,v} \delta i_{u+\delta u, v+\delta v} \rangle (\boldsymbol{\theta})}{N(\delta u, \delta v)}. \tag{4}$$

$\sum_{u,v}$ denotes a summation over all pairs of subapertures with separation $\boldsymbol{\rho} = (\delta u, \delta v)$ and $N(\delta u, \delta v)$ represents the number of pairs of such subapertures. The pseudo-measurements given by Eqs. (3) and (4) are then stacked into a single vector $\mathbf{C_{mes}}$, related to the discretized $C_n^2$ profile at different altitudes $\mathbf{C_n^2}$, by the following linear relationship:

$$\mathbf{C_{mes}} = M\mathbf{C_n^2} + \mathbf{C_d} + \mathbf{u}. \tag{5}$$

$M$ is the matrix of the weighting functions $W_{ss}^{kk}$ and $W_{ii}$ of Eqs. (1) and (2). Because slope and scintillation data are affected by detection noises, the pseudo-measurements $\mathbf{C_{mes}}$ are biased with the averaged correlations of these noises $\mathbf{C_d}$. As we estimate the correlations from a finite number of frames, $\mathbf{u}$ represents a convergence noise, which we assume to be Gaussian in the following.

## 2.3. Maximum Likelihood solution

The $C_n^2$ profile is retrieved by minimizing the following Maximum Likelihood (ML) criterion, which is the opposite of the data log-likelihood [16]:

$$J_{\mathrm{ML}}\left(\mathbf{C_n^2}\right) = \left(\mathbf{C_{mes}} - \mathbf{C_d} - M\mathbf{C_n^2}\right)^{\mathrm{T}} C_{\mathrm{conv}}^{-1} \left(\mathbf{C_{mes}} - \mathbf{C_d} - M\mathbf{C_n^2}\right). \tag{6}$$

Under the adopted Gaussian assumption for the convergence noise, this criterion is quadratic and its unconstrained minimization thus has an analytical solution. Yet, as the $C_n^2$ is always non-negative, we minimize $J_{\mathrm{ML}}$ under positivity constraint, using a VMLM - B (Variable Metric with Limited Memory-and-Bounds) algorithm [17]. The covariance matrix of the convergence noise $\mathbf{u}$, $C_{\mathrm{conv}} = \langle \mathbf{uu^T} \rangle$, is deduced from an analytical expression depending on the theoretical correlations, which are in practice approximated with the pseudo-measurements [18]. The idea of the derivation of $C_{\mathrm{conv}}$ can be gained from examining the scalar case of a single variable. To this aim, Appendix A gives the calculation of the variance of the convergence noise for a centered Gaussian random variable.

Two methods are considered to take into account the bias due to detection noises $\mathbf{C_d}$. Assuming that the noises are not correlated between the two directions of observation and between different subapertures, only the variances of slopes and of scintillation are biased. These variances are averaged over all subapertures and represent the central point of the auto-correlation maps. Three new parameters, *i.e.* the variances of the noises on $x$-slopes, $y$-slopes and scintillation, can be estimated jointly with the $C_n^2$ profile, without changing the ML criterion given by Eq. (6). Another option is to exclude the variances of slopes and of scintillation from the vector $\mathbf{C_{mes}}$. These two methods will be tested and compared further.

Using Eq. (6), the error covariance matrix of the ML estimation can be shown [16] to be $\mathrm{cov}\left(\hat{\mathbf{C}}_{\mathbf{n}_{\mathrm{ML}}}^{\mathbf{2}}\right) = \left(M^{\mathrm{T}}C_{\mathrm{conv}}^{-1}M\right)^{-1}$ and can be used to obtain error bars on the restored profile. Indeed, the diagonal values of this matrix represent the variances of the estimates of the $C_n^2$ as a function of altitude, from which $3\sigma$ error bars are easily computed and will be considered as an upper bound of the error on the reconstructed profile.

## 2.4. Maximum A Posteriori solution

As the $C_n^2$ profile is supposed to be smooth near the ground, we can also minimize a Maximum *A Posteriori* (MAP) metric [16] composed of the ML criterion $J_{\mathrm{ML}}$ and a regularization metric, denoted hereafter by $J_{\mathrm{p}}$ and designed to enforce smoothness of the $C_n^2$ profile:

$$J_{\mathrm{MAP}}\left(\mathbf{C_n^2}\right) = \left(\mathbf{C_{mes}} - \mathbf{C_d} - M\mathbf{C_n^2}\right)^{\mathrm{T}} C_{\mathrm{conv}}^{-1} \left(\mathbf{C_{mes}} - \mathbf{C_d} - M\mathbf{C_n^2}\right) + J_{\mathrm{p}}\left(\mathbf{C_n^2}\right). \tag{7}$$

In this paper, we take:

$$J_{\mathrm{p}}\left(\mathbf{C_n^2}\right) = \beta ||\nabla \mathbf{C_n^2}||^2, \tag{8}$$

where $\beta$ is a regularization parameter and $\nabla$ represents the gradient operator. With this kind of regularization, the constraint applies mainly on strong turbulent layers, located near the ground.

Later in this article, we will use either the ML or the MAP solution.

## 2.5. Altitude resolution

In cross-correlation methods, simple geometrical rules are used to define the altitude resolution $\delta h$ of the instrument. For SLODAR, we have [5]:

$$\delta h \simeq \frac{d_{\mathrm{sub}}}{\theta}, \tag{9}$$

where $d_{sub}$ is the subaperture diameter. For G-SCIDAR, we have [9, 19]:

$$\delta h \simeq 0.78 \frac{\left( \lambda \left| h - h_{gs} \right| \right)^{1/2}}{\theta},$$  (10)

where $\lambda$ is the observation wavelength and $h_{gs}$ the extra-propagation length. For both methods, the maximum altitude of sensitivity $H_{max}$ is constrained by the telescope diameter $D$ and the star separation $\theta$ and is written as [5]:

$$H_{max} \simeq \frac{D}{\theta}.$$  (11)

In this paper, the altitude sampling and the maximum altitude of sensitivity of the CO-SLIDAR will be given by Eqs. (9) and (11) as we use a SH, like in the SLODAR method.

## 3. Simulation results

In this section, we present the results of a numerical simulation in a practical astronomical case. In Subsection 3.1 we describe the simulation and we show the resulting correlation maps. In Subsection 3.2, we estimate the $C_n^2$ profiles and discuss the results.

### 3.1. Simulated data and correlation maps

We consider a $30 \times 30$ SH, conjugated with a telescope of diameter $D = 1.5$ m with a central obscuration of 30 %. The subaperture diameter is $d_{sub} = 5$ cm. The object is a binary star with separation $\theta = 20$", observed at $\lambda = 0.55$ $\mu$m. The two stars have a difference of one magnitude and the fluxes are about 120 and 300 photons per subaperture and per frame. We use a $C_n^2$ profile sampled on 32 layers every 625 m. This profile corresponds to a Fried parameter $r_{0_{th}} \simeq 5.5$ cm, and a variance of log-amplitude $\sigma_{\chi_{th}}^2 \simeq 0.023$.

Typical SH noisy images obtained after propagation through von Kármán turbulence are shown in Fig. 1. The detector read-out noise is $\sigma_{e^-} = 1$ e$^-$/pixel. More details on the image simulation process are given in [13].



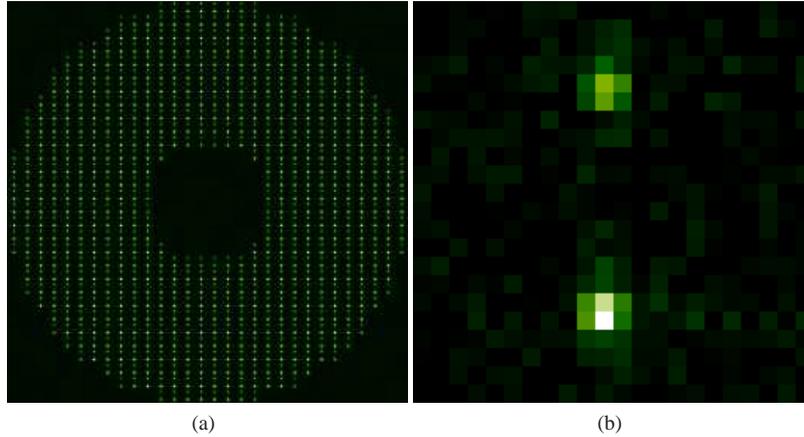(a)                                                                    (b)

Fig. 1. Example of simulated Shack-Hartmann turbulent and noisy images. (a) Full Shack-Hartmann long-exposure image. (b) Subaperture short-exposure image.

Slopes and intensity fluctuations are extracted from the turbulent images. Slopes are measured using a center of gravity (COG) algorithm, in windows of $8 \times 8$ pixels, centered on the maximum of each star. We do not use smaller windows because doing so introduced a bias on the $C_n^2$ profile reconstruction. Here, we cannot use larger windows either to avoid mixing the two stars' signals. The intensities, from which we deduce the intensity fluctuations, correspond to the sum of all pixel intensities included in the windows.

Then we build correlation maps, presented in Fig. 2. These maps show the correlation averaged over all pairs of subapertures with given separation. The auto-correlation maps have a
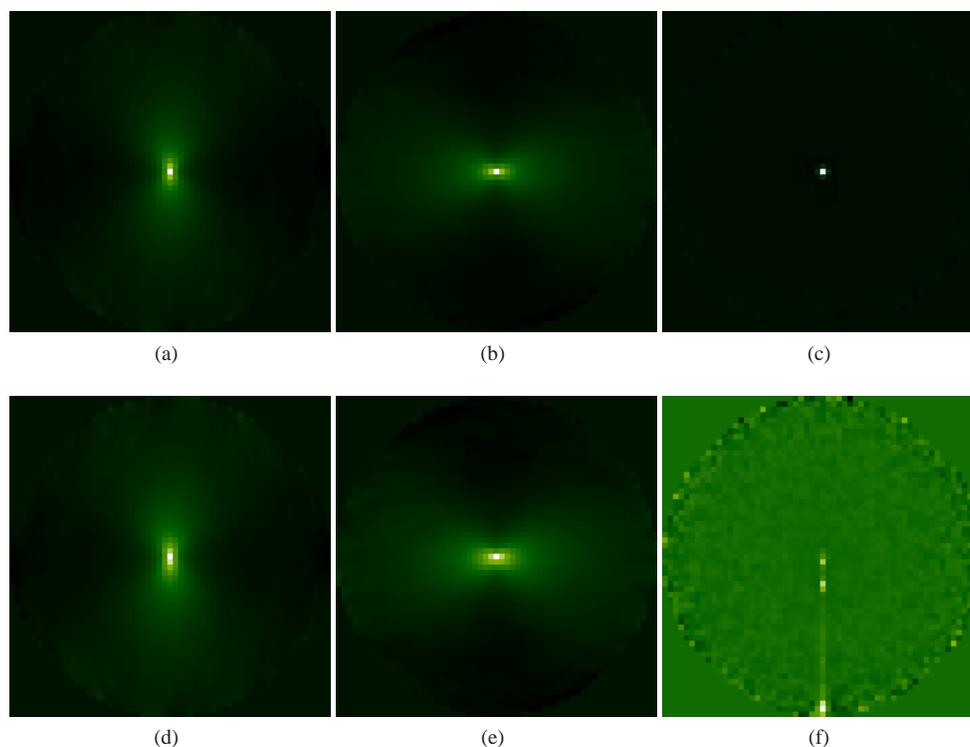


Fig. 2. Correlation maps from simulated slope and scintillation data. One pixel of these maps shows the correlation averaged over all pairs of subapertures with given separation. (a), (b), (c) Auto-correlation maps. (d), (e), (f) Cross-correlation maps. (a), (d) Correlations of $x$-slopes. (b), (e) Correlations of $y$-slopes. (c), (f) Correlations of scintillation.

maximum at their center. They represent the response of the system to the integral of turbulence. We can notice that the scintillation response is very narrow compared to the slope response. In the cross-correlation maps, the peak of correlation associated to the turbulent layer at altitude $h$ is centered on $\boldsymbol{\rho} = \boldsymbol{\theta}h$. In the cross-correlation map of scintillation, the peaks of correlation associated to the turbulent layers at different altitudes are visible in the bottom part of the map, in the alignment direction of the stars. In the cross-correlation maps of slopes, only the peak of correlation corresponding to $h = 0$ is visible, at the center of the map. The peaks of correlation associated to the other layers are also located at $\boldsymbol{\theta}h$, but because of the width of the response and its decreasing strength with altitude, they are not visible to the naked eye.

In CO-SLIDAR, we use both slope and scintillation responses to be sensitive to low and high

altitude turbulent layers.

## 3.2. Reconstruction of the $C_n^2$ profiles

We now use the ML solution to retrieve the $C_n^2$ profile. Here, $\delta h \simeq 500$ m, and $H_{max} \simeq 15$ km, according to Eqs. (9) and (11). The detection noise bias is estimated jointly with the $C_n^2$ profile and subtracted. We estimate 32 layers, with the same altitude sampling as for the theoretical $C_n^2$ input profile. The results presented in Fig. 3 are compared to profiles reconstructed from
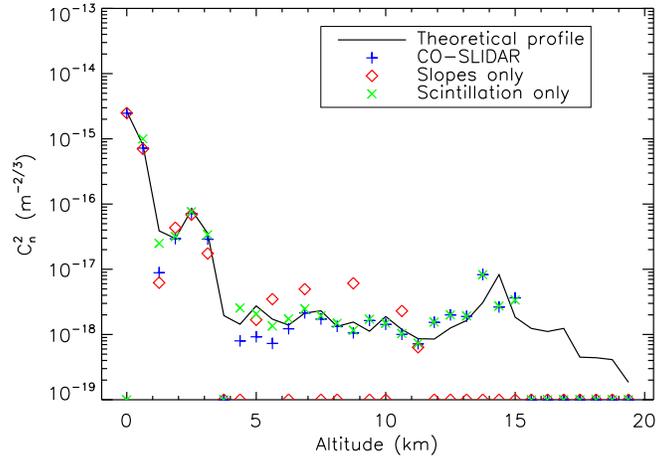


(a)
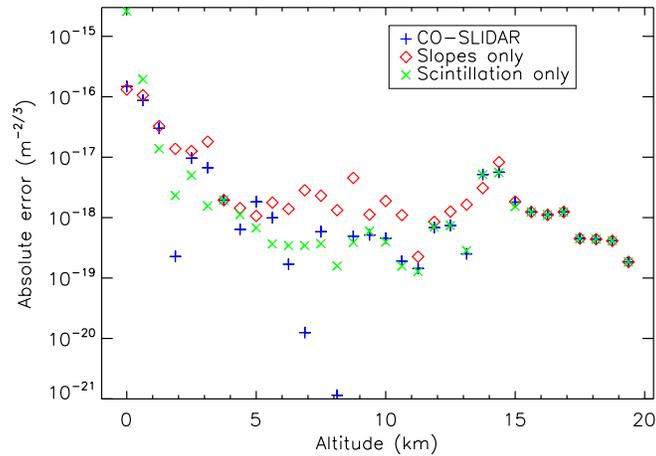


(b)

Fig. 3. (a) ML reconstruction of the $C_n^2$ profile from correlations of slopes only, of scintillation only and with the CO-SLIDAR method, in simulation. In all cases, the detection noise bias has been estimated jointly with the $C_n^2$ profile. (b) Absolute error on the reconstruction.

correlations of slopes only or of scintillation only. Because of the positivity constraint, some values are estimated to zero by the estimator. They are arbitrarily set to $10^{-19}$ m$^{-2/3}$ for the display. We also plot the absolute error on the reconstruction denoted $|\left(C_{n_{est}}^2\left(h_i\right) - C_{n_{th}}^2\left(h_i\right)\right)|$. $C_{n_{est}}^2\left(h_i\right)$ is the estimated $C_n^2$ at altitude $h_i$ ($i \in [1\,;\,32]$) and $C_{n_{th}}^2\left(h_i\right)$ is the true $C_n^2$ at altitude $h_i$. In this figure, we see that correlations of slopes allow a good reconstruction of ground and low altitude layers, but provide a poor resolution at high altitude (alternation of strong and zero values) and no sensitivity at all above 12 km. Conversely, correlations of scintillation lead to a good reconstruction at low and high altitude, but they do not allow the estimation of the ground layer.

CO-SLIDAR takes advantage of both correlations of slopes and of scintillation, leading to a more complete reconstruction of low and high altitude layers. CO-SLIDAR, as well as the other methods, does not succeed in estimating layers over 15 km, altitude which corresponds to $H_{max}$ in this simulation. The Fried parameter estimated from the CO-SLIDAR $C_n^2$ profile is $r_0 \simeq 5.8$ cm and the estimated variance of log-amplitude is $\sigma_\chi^2 \simeq 0.020$. These values are very close to the true ones: $r_{0_{th}} \simeq 5.5$ cm, $\sigma_{\chi_{th}}^2 \simeq 0.023$.

In Table 1, we present the Root Mean Square Error (RMSE), for each reconstruction of the $C_n^2$ profile and for different altitude slices, defined as:

$$RMSE = \left(\frac{1}{N_l}\sum_{i=1}^{N_l}\left(C_{n_{est}}^2\left(h_i\right) - C_{n_{th}}^2\left(h_i\right)\right)^2\right)^{1/2}, \tag{12}$$

where $N_l$ is the number of layers considered. We divided the profile into three altitude slices: the first two layers, the next four layers, and the remaining high altitude layers. As the reconstruction from correlations of scintillation only is not sensitive to the ground layer, we only consider the second layer to calculate the RMSE in the first altitude slice.

Table 1. RMSE in function of the altitude slice for the ML reconstruction of the $C_n^2$ profile, from correlations of slopes only, of scintillation only, and with the CO-SLIDAR method.

| | First two layers (Second layer) | Four next layers | High altitude layers |
|---|---|---|---|
| Slopes only (m$^{-2/3}$) | $1.2 \times 10^{-16}$ $\left(1.1 \times 10^{-16}\right)$ | $2.1 \times 10^{-17}$ | $2.4 \times 10^{-18}$ |
| Scintillation only (m$^{-2/3}$) | not applicable $\left(1.9 \times 10^{-16}\right)$ | $7.5 \times 10^{-18}$ | $1.7 \times 10^{-18}$ |
| CO-SLIDAR (m$^{-2/3}$) | $1.2 \times 10^{-16}$ $\left(8.7 \times 10^{-17}\right)$ | $1.6 \times 10^{-17}$ | $1.7 \times 10^{-18}$ |

The results in Table 1 show that for the first two layers, the CO-SLIDAR reconstruction is similar to the reconstruction from correlations of slopes and better than the reconstruction from correlations of scintillation. For high altitude layers, the CO-SLIDAR reconstruction is similar to the reconstruction from correlations of scintillation and better than the reconstruction from correlations of slopes. For the four layers between 1.25 and 3.125 km, the CO-SLIDAR reconstruction is better than the reconstruction from correlations of slopes, but is surprisingly worse than the reconstruction from correlations of scintillation. In principle, using more data should not decrease the quality of the reconstruction. This effect is possibly due to the fact that we *estimate* the covariance matrix of the convergence noise $C_{conv}$ using the pseudo-measurements. It should be investigated in more details in a future work.

The two methods to subtract the detection noise bias are now compared in Fig. 4 for the CO-SLIDAR reconstruction. In one case, as previously explained, we estimate the detection noise
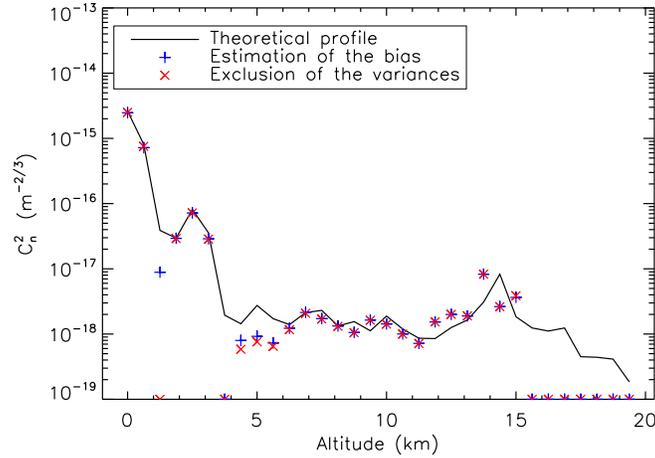


Fig. 4. ML CO-SLIDAR reconstruction of the $C_n^2$ profile, with joint estimation of the detection noise bias and with exclusion of the variances from the direct problem, in simulation.

bias jointly with the turbulence profile, whereas in the other case we simply exclude the noisy pseudo-measurements, *i.e.* the variances of slopes and of scintillation, from the direct problem.

In the joint estimation, the variances of noises that we estimated were close to the expected ones ($\sigma_{s_{n\text{-th}}^x}^2 = 0.26$ rad$^2$, $\sigma_{s_{n\text{-th}}^y}^2 = 0.28$ rad$^2$, $\sigma_{\delta i_{n\text{-th}}}^2 = 8.7 \times 10^{-3}$), but slightly higher ($\sigma_{s_{n\text{-est}}^x}^2 = 2.8$ rad$^2$, $\sigma_{s_{n\text{-est}}^y}^2 = 0.32$ rad$^2$, $\sigma_{\delta i_{n\text{-est}}}^2 = 1.2 \times 10^{-2}$). By subtracting the expected values from the estimated ones, we found a residual term. We noted that this term was identical to the one retrieved by the estimator when performing joint estimation with data free from detection noises ($\sigma_{s_{n\text{-res}}^x}^2 = 3,7 \times 10^{-2}$ rad$^2$, $\sigma_{s_{n\text{-res}}^y}^2 = 5,7 \times 10^{-2}$ rad$^2$, $\sigma_{\delta i_{n\text{-res}}}^2 = 3,1 \times 10^{-3}$). Moreover, we noticed in our simulations that the reconstruction of the $C_n^2$ profile from data free from detection noise was more accurate when estimating the bias. Therefore this small residual term can be identified as the one corresponding to model errors (for example, in the simulation, the error due to the size of the window for the measurements). Thus, the joint estimation method allows one to estimate accurately the $C_n^2$ profile and the variances of noises, and is capable of estimating biases other than those due to detection noises, adding extra degrees of freedom to the estimation.

In the second method, we discard the variances of slopes and of scintillation from the pseudo-measurements. When we compare the two methods, we find that they give very similar results and allow a good reconstruction of the turbulent profile, so we have two efficient methods to subtract the bias due to detection noises.

Then we compute the $3\sigma$ error bars, and we represent them together with the estimated profile, as shown in Fig. 5. The $C_n^2$ profile is retrieved with the joint estimation method. We note that the relative error, defined as the absolute error divided by the $C_n^2$ value at a given altitude, is weaker for turbulent layers with strong $C_n^2$ values and low altitudes. Indeed, these layers correspond to a better signal to noise ratio (SNR). Moreover, cross-correlations corresponding to these altitudes are estimated with a larger number of samples, because they are associated to more pairs of subapertures. Finally, we can see that the true $C_n^2$ profile is well included within
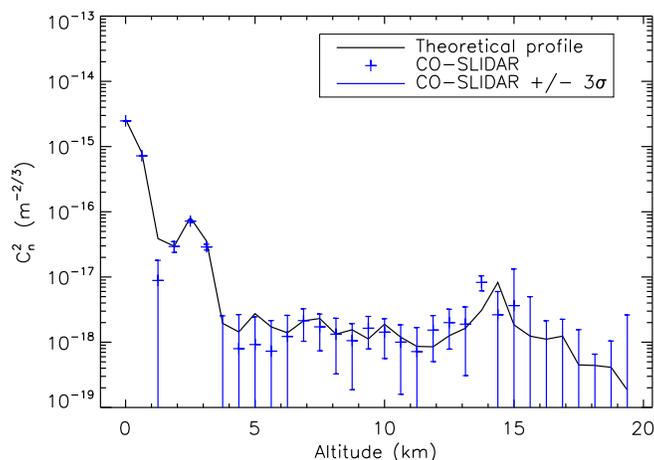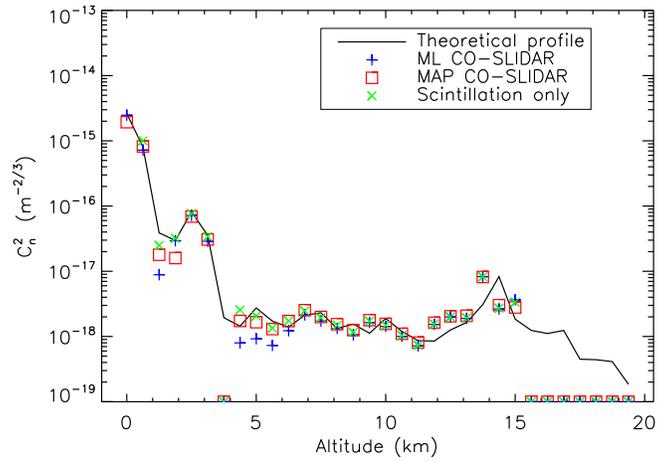
Fig. 5. ML CO-SLIDAR reconstruction of the $C_n^2$ profile, with joint estimation of the detection noise bias, and with the estimated $3\sigma$ error bars, in simulation.

these $3\sigma$ error bars, excepted the layers located at 1.25 and 13.75 km.

In Fig. 6, we finally compare the ML CO-SLIDAR reconstruction of the $C_n^2$ profile with the reconstruction from correlations of scintillation only and with the MAP CO-SLIDAR reconstruction for a weakly regularized case. The regularization parameter $\beta$ has been chosen so that the likelihood and the prior terms of Eq. (7) have approximately the same order of magnitude. We have increased it until the estimation of the ground layer, on which there is a very good SNR, begins to be biaised towards zero. Note that this tuning strategy is also applicable to experimental data. We also plot the absolute error on the reconstruction. In this figure, we see that the MAP $C_n^2$ profile is smoother than the ML profile as expected. We note slight differences between the ML and the MAP profiles but the two approaches allow a good reconstruction, as quantified by Table 2.

In Table 2, we present the Root Mean Square Error (RMSE) for the ML and MAP CO-SLIDAR reconstructions and for the reconstruction from correlations of scintillation only. The results in Table 2 show that for the first two layers, the MAP reconstruction is still better than the reconstruction from correlations of scintillation only, but worse than the ML reconstruction. This is due to this kind of regularization, where the constraint applies mainly on strong turbulent layers. In contrast, the reconstruction of high altitude layers is slightly better with the MAP solution than with the ML solution and than the reconstruction from correlations of scintillation only. For the layers between 1.25 and 3.125 km, the reconstruction from correlations of scintillation is still better, probably for the reasons previously mentioned. To improve the accuracy of the MAP estimation, we could use an adaptive regularization [20], designed to take into account the dynamic range of the $C_n^2$ profile.

We have shown in this section that CO-SLIDAR gives good results in simulation, and allows one to estimate the $C_n^2$ profile over the whole range of altitudes, with a sub-kilometric resolution. The next step is to examine its on-sky performance.

(a)
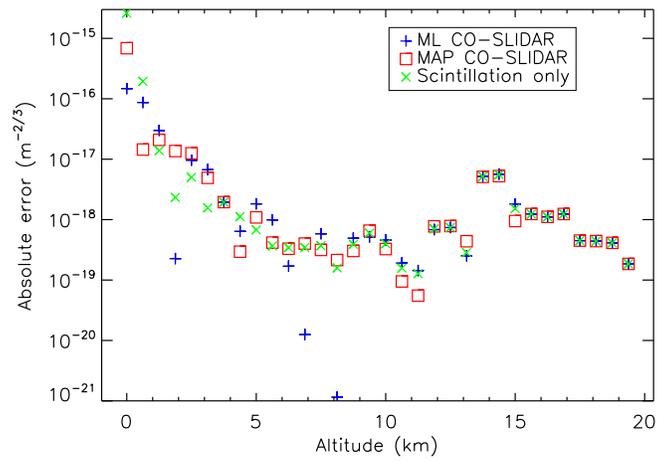


(b)

Fig. 6. (a) ML and MAP CO-SLIDAR reconstructions of the $C_n^2$ profile and comparison with the reconstruction from correlations of scintillation only, in simulation. (b) Absolute error on the reconstruction.

Table 2. RMSE in function of the altitude slice, for the reconstruction of the $C_n^2$ profile from correlations of scintillation only and for the ML and MAP CO-SLIDAR reconstructions.

| | First two layers (Second layer) | Four next layers | High altitude layers |
|---|---|---|---|
| Scintillation only ($m^{-2/3}$) | not applicable $(1.9 \times 10^{-16})$ | $7.5 \times 10^{-18}$ | $1.7 \times 10^{-18}$ |
| ML CO-SLIDAR ($m^{-2/3}$) | $1.2 \times 10^{-16}$ $(8.7 \times 10^{-17})$ | $1.6 \times 10^{-17}$ | $1.7 \times 10^{-18}$ |
| MAP CO-SLIDAR ($m^{-2/3}$) | $4.9 \times 10^{-16}$ $(1.4 \times 10^{-17})$ | $1.4 \times 10^{-17}$ | $1.6 \times 10^{-18}$ |

## 4. On-sky results

In this section we describe the on-sky experiment and present the very first on-sky results of the CO-SLIDAR instrument. In Subsection 4.1 we detail the CO-SLIDAR instrument. Subsection 4.2 is dedicated to observations and data analysis. The estimated $C_n^2$ profiles are shown in Subsection 4.3. These CO-SLIDAR profiles are compared to $C_n^2$ profiles deduced from NCEP/NCAR Reanalysis in Subsection 4.4.

### 4.1. The CO-SLIDAR instrument

The experiment took place on the Plateau de Calern, at the Observatoire de la Côte d'Azur, near Nice, France. We used the 1.5 m MeO telescope, with a central obscuration of 30 %, coupled to a $30 \times 30$ subaperture SH, hence the subaperture diameter is $d_{sub} = 5$ cm. The CO-SLIDAR instrument was mounted behind the Coudé train of the telescope, composed of seven mirrors and one doublet. Two lenses of focal lengths 800 mm and 56 mm were used to image the telescope pupil onto the $30 \times 30$ lenslet array. The microlens array had a pitch of 143 $\mu$m and a focal length of 3.6 mm. As it was too short to form an image directly on the detector array, we used an additional pair of lenses of focal lengths 120 mm and 150 mm to transfer the focal plane. The observation wavelength was $\lambda = 517$ nm, with $\Delta\lambda = 96$ nm. The camera used was an Andor-iXon3-885 electron multiplication CCD (EMCCD) with a quantum efficiency of about 50 %, and a detector read-out noise close to one e$^-$/pixel. The final plate scale on the SH is 1.2 arcsec/pixel.

### 4.2. Observations and data analysis

Observations were done on May 2012, on the double star Mizar AB. We selected the data from May, 15$^{th}$, around 01:00 UT. The zenith angle of the binary star was $\zeta = 35°$. The exposure time was $t_{exp} = 3$ ms, to freeze the turbulence. The separation between the two components is $\theta = 14.4$" and their visible magnitudes are 2.23 and 3.88, leading to about 260 and 60 photons per subaperture and per frame. We recorded sequences of 1000 images at 15 Hz, so the sequence duration is about 1 min. Typical on-sky images are shown in Fig. 7.

We extract slopes and scintillation from these images, in windows of $9 \times 9$ pixels. We check the statistics of turbulence with the two kinds of data. From slopes we compute the Zernike coefficient variances, showing a Kolmogorov turbulence with an outer scale effect, noticeable on the tip-tilt. We check the hypothesis of the weak perturbation regime using intensities and intensity fluctuations, by fitting a log-normal distribution and estimating $\sigma^2_{\chi_{data}}$. The latter was found to be far below 0.3, validating the hypothesis of weak perturbations.
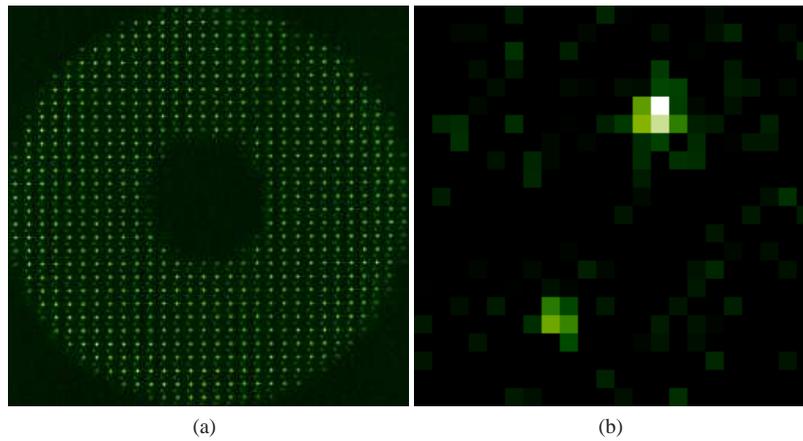
(a)　　　　　　　　　(b)

Fig. 7. Experimental Shack-Hartmann turbulent images, for a 3 ms exposure time. (a) Full Shack-Hartmann long-exposure image. (b) Subaperture short-exposure image.



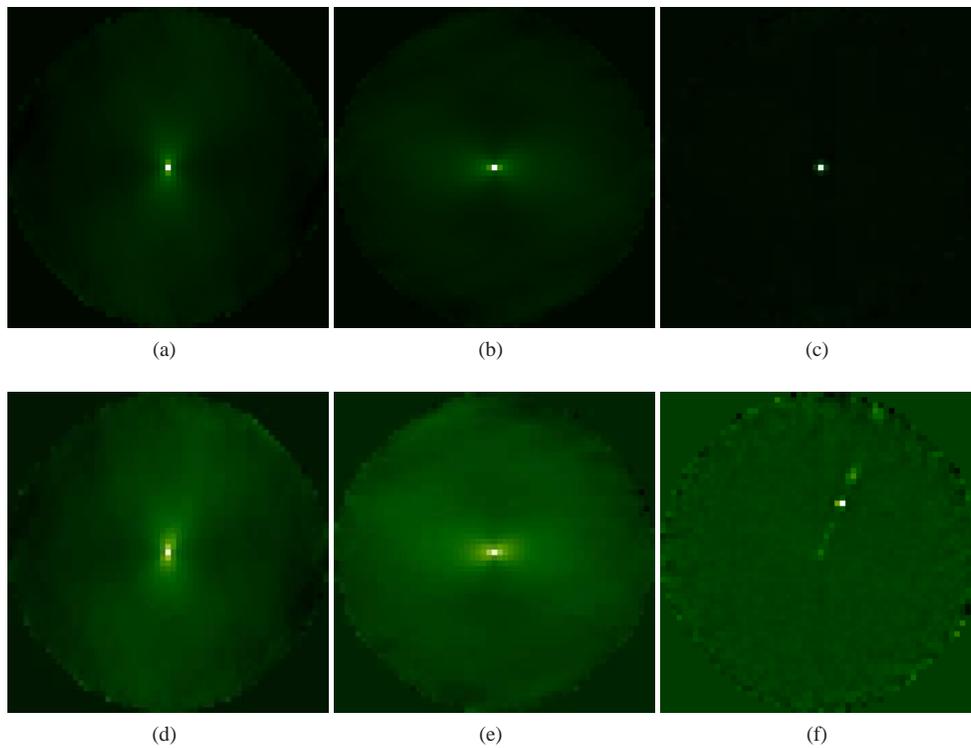(a)　　　　　　　(b)　　　　　　　(c)

(d)　　　　　　　(e)　　　　　　　(f)

Fig. 8. Correlation maps from experimental slope and scintillation data. (a), (b), (c) Auto-correlation maps. (d), (e), (f) Cross-correlation maps. (a), (d) Correlations of *x*-slopes. (b), (e) Correlations of *y*-slopes. (c), (f) Correlations of scintillation.

The correlation maps in Fig. 8 present a pattern similar to the one obtained in the simulation. The cross-correlation map of scintillation shows peaks of correlation in the top right quarter of the map, in the alignment direction of the stars, representing the turbulent layers' signatures. The comments on the other maps are the same as in the simulation case.

These verifications confirm the data consistency with the model hypotheses and that we can use the pseudo-measurements to estimate the $C_n^2$ profiles.

### 4.3. Estimation of the turbulence profiles

As we use a von Kármán model for turbulence, we have to choose an outer scale $L_0$. We assume that $L_0 = 27$ m, which is the median outer scale observed at the Plateau de Calern [21]. We checked that the results were not significantly affected by the outer scale choice in the range $[10 \, ; 50]$ m and we found very similar $C_n^2$ profiles. We estimate 30 layers. Here, $\delta h \simeq 600$ m and $H_{\max} \simeq 17$ km, using Eqs. (9) and (11), corrected from the zenith angle $\zeta$.
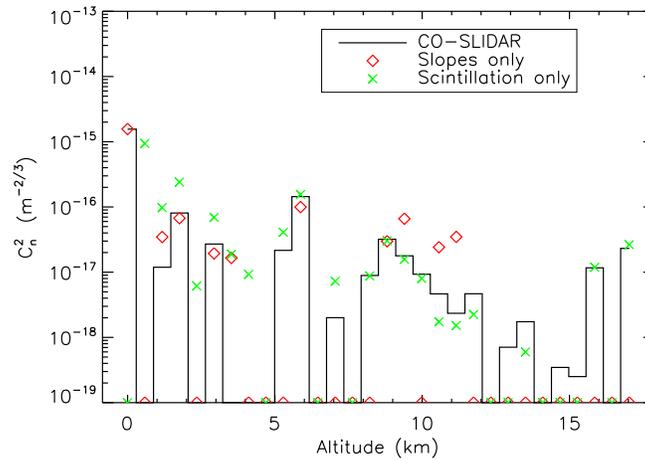


Fig. 9. ML reconstruction of the $C_n^2$ profile from correlations of slopes only, of scintillation only and with the CO-SLIDAR method. 1 min dataset acquired around 01:00 UT, on May $15^{th}$, 2012, with a 3 ms exposure time. In all cases, the detection noise bias has been estimated jointly with the $C_n^2$ profile.

The $C_n^2$ profiles are estimated with the ML solution, from correlations of slopes only, of scintillation only and with the CO-SLIDAR method. For each reconstruction, the detection noise bias is estimated jointly with the $C_n^2$ profile. The results are presented in Fig. 9. At high altitude, we find a good agreement between the CO-SLIDAR reconstruction and that from correlations of scintillation. As in the simulated case, the turbulence estimated from correlations of slopes is somewhat different, alternation of stronger and zero values. At low altitude, we observe a good agreement between the CO-SLIDAR reconstruction and that from correlations of slopes, the turbulence estimated from correlations of scintillation being stronger. However without any true profile, it is difficult to discard this solution.

In Fig. 10, we compare the ML CO-SLIDAR $C_n^2$ profiles reconstructed with joint estimation of the detection noise bias, and with exclusion of the variances from the direct problem. We obtained very similar results with the two estimations. We note that the $C_n^2$ values estimated when discarding the variances are slightly higher than when we estimate the noise detection
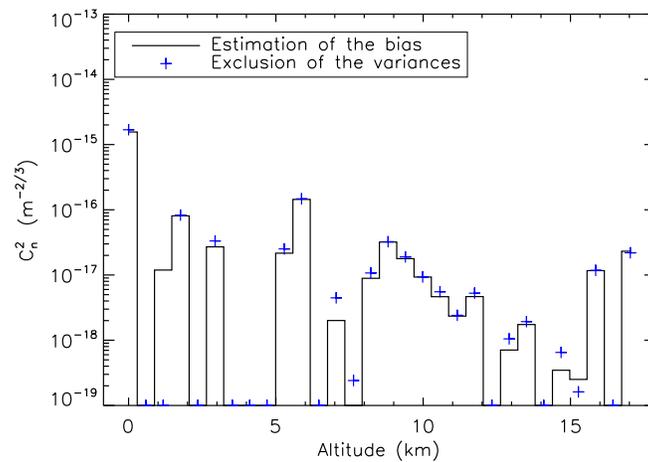
Fig. 10. ML CO-SLIDAR reconstruction of the $C_n^2$ profile, with joint estimation of the detection noise bias and with exclusion of the variances from the direct problem. 1 min dataset from May $15^{th}$, 2012, around 01:00 UT.

bias. In the following, we will always use the joint estimation to reconstruct the $C_n^2$ profile.

Following these encouraging results we perform a MAP estimation in order to impose some smoothness to the profile reconstruction. We use the same regularization parameter as in the simulation case, because the $C_n^2$ profile is of the same order of magnitude and has a similar shape. The corresponding $C_n^2$ profile is presented in Fig. 11 and compared to the one without regularization. We get a slightly different profile from the ML one, smoother in the first kilometer. The differences occur mainly at low altitudes, from 0 to 4 km.
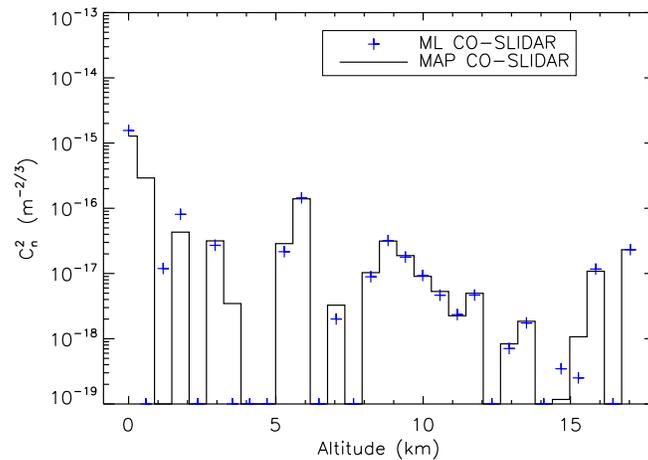


Fig. 11. ML and MAP CO-SLIDAR reconstructions of the $C_n^2$ profile. 1 min dataset from May $15^{th}$, 2012, around 01:00 UT.

Finally, in Fig. 12 we add the $3\sigma$ error bars on the reconstructed profile and we present three MAP $C_n^2$ profiles corresponding to three consecutive minutes of observation, each profile corresponding to one minute of observation. The three profiles are very similar. They show strong turbulence at low altitude, another strong layer around 5 km, and some weaker layers in altitude. This shape of turbulence profile is typical of an astronomical site. The mean Fried parameter estimated on the line of sight is $r_0 \simeq 6.9$ cm, and the mean variance of log-amplitude is $\sigma_\chi^2 \simeq 0.045$.

### 4.4. Comparison with $C_n^2$ profiles deduced from NCEP/NCAR Reanalysis

We compare the CO-SLIDAR estimation with a free atmosphere $C_n^2$ profile deduced from NCEP/NCAR Reanalysis. This method does not allow an estimation of the turbulence in the boundary layer, as meteorological parameters are too unstable in this part of the atmosphere.

As they are very similar, we only consider the second $C_n^2$ profile of those reconstructed throughout the three consecutive minutes with the MAP estimation, around 01:00 UT, on May 15th, 2012. This profile is compared with the free atmosphere $C_n^2$ profile at 00:00 UT and with the mean profile of May 2012, obtained from NCEP/NCAR Reanalysis. The comparison is shown in Fig. 13. The turbulence profiles computed from NCEP/NCAR Reanalysis are very smooth, because they correspond to an averaging of the data, so they cannot show fast changes in the $C_n^2$ profile, unlike the CO-SLIDAR method.

A few differences can be noticed between the profile at 00:00 h UT and the mean profile deduced from NCEP/NCAR Reanalysis, but their shape are very similar.

The CO-SLIDAR $C_n^2$ profile and those obtained from NCEP/NCAR Reanalysis are of the same order of magnitude. Between 1 and 5 km, the estimation from NCEP/NCAR Reanalysis is lower than the CO-SLIDAR one, whereas between 6 and 15 km it is the opposite. Both estimations show a decrease of the turbulence strength between 9 and 15 km. Between 16 and 17 km, the CO-SLIDAR estimation presents a rise of the turbulence strength, contrary to the estimation from NCEP/NCAR Reanalysis. This rise with the CO-SLIDAR estimation could correspond to the integral of unseen turbulence above 17 km, while this turbulence is reconstructed with the estimation from NCEP/NCAR Reanalysis. This rise could also be an artefact because these very high altitudes correspond to the edge of the cross-correlation maps, where the SNR is poor and where we have few pairs of subapertures to estimate the correlations.

The CO-SLIDAR $C_n^2$ profiles have been found to be comparable on average to the $C_n^2$ profiles for the free atmosphere deduced from NCEP/NCAR Reanalysis, despite the difference of the two methods, from the kind of data they use, to the way they work.

## 5. CO-SLIDAR in the $C_n^2$ profilers' landscape

The results presented in the previous section confirm that CO-SLIDAR on meter class telescopes provides sub-kilometric resolution $C_n^2$ profiles in the $[0 ; 20]$ km altitude range. This method could be used for site characterization to obtain relevant inputs for tomographic AO design and performance evaluation, or to help optical turbulence forecast.

Of course, inter-comparisons are needed, with the reference profilers SLODAR, G-SCIDAR and MASS, and with new-generation profilers, such as PML (Profiler of Moon Limb) [22] and Stereo-SCIDAR [23]. A multi-instrument campaign dedicated to this comparison is foreseen [24].

Tomographic AO systems will include several wavefront sensors, leading to multi-directional SLODARs [25, 26, 27], but external $C_n^2$ profilers such as CO-SLIDAR would be useful for the calibration of these systems.
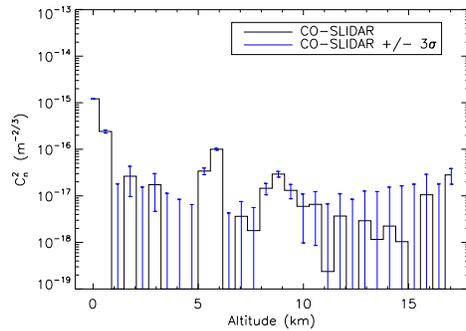
Moreover, some hardware and architecture improvements are possible on the CO-SLIDAR instrument. The optical transmission could be increased and the sources could be separated on
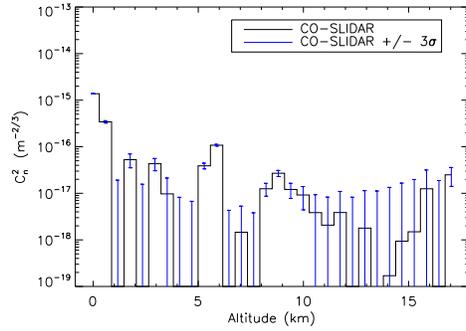
(a)
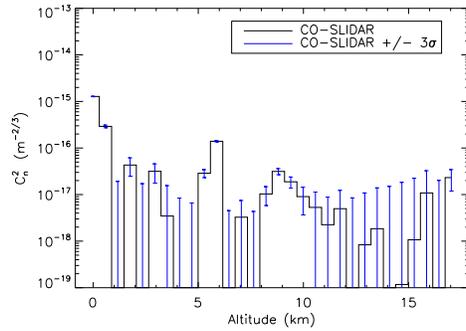


(b)



(c)

Fig. 12. (a), (b), (c) MAP CO-SLIDAR reconstructions of the $C_n^2$ profile with the estimated $3\sigma$ error bars, for three consecutive minutes of observation. Each profile corresponds to one minute of observation. Data from May $15^{th}$, 2012, around 01:00 UT.
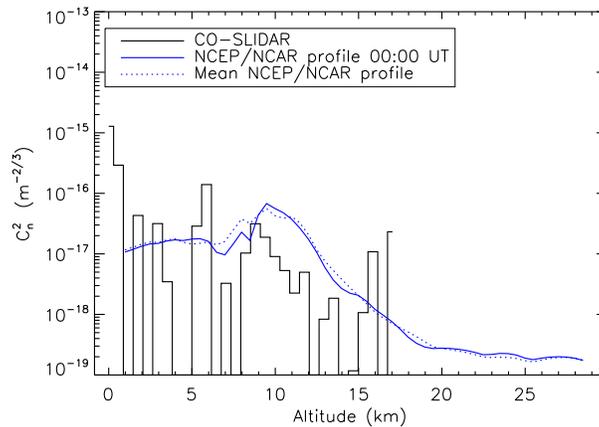
Fig. 13. MAP CO-SLIDAR reconstruction of the $C_n^2$ profile. 1 min dataset from May $15^{th}$, 2012, around 01:00 UT. Comparison with the free atmosphere profile at 00:00 UT and with the mean profile of May 2012, deduced from NCEP/NCAR Reanalysis.

two different detectors to tune the detector gain on each star, to observe binary stars with visible magnitude up to 6 and thus to allow a better sky coverage. With two detectors the images' size would be smaller and that would speed up their recording, to enable wind profiling. Outer scale profiling is also possible. Eventually, CO-SLIDAR could be used as an automatic monitor, by means of real time data processing.

## 6. Conclusion

In this paper, we have presented the first-on sky $C_n^2$ profiles estimated with the CO-SLIDAR profiler. The improved reconstruction method has been described and its latest performance has been illustrated in an end-to-end simulation, before testing it in a real astronomical observation on the 1.5 m MeO telescope. $C_n^2$ profiles have been estimated with the CO-SLIDAR method and compared to those reconstructed from correlations of slopes only or of scintillation only, highlighting the fact that the two kinds of correlations are complementary and allow the reconstruction of low and high altitude layers. With this CO-SLIDAR instrument, we have reconstructed 30 turbulent layers, with a resolution of 600 m, from the ground up to 17 km. We have compared our results with the $C_n^2$ profiles deduced from NCEP/NCAR Reanalysis, and we have found a good agreement between the estimations. In a nutshell, we have shown that CO-SLIDAR is a sub-kilometric resolution $C_n^2$ profiler working on meter class telescopes. The method now needs cross-calibrations with other optical profilers in multi-instrument campaigns. Considered future works include improvements to gain a better sky-coverage, performing real-time $C_n^2$ estimations, and extensions to wind and outer scale profiling.

## A. Estimation of the variance of the convergence noise for a Gaussian random variable

In CO-SLIDAR, the correlations are estimated from a finite number of frames. The so-called convergence noise corresponds to the difference between these empirical estimations and the exact mathematical expectations.

In this appendix, we illustrate the methodology for computing $C_{\text{conv}}$ in the simplified case of the estimation of the variance of a scalar Gaussian random variable by expressing the variance

of the convergence noise.

Let $X$ be a centered Gaussian random variable such as $X \sim \mathcal{N}\left(0, \sigma_X^2\right)$ and $x_i$ a realization of $X$. An estimation of the variance of $X$, $\sigma_X^2$ (which is a ML estimate because we have assumed $X$ to be Gaussian), is given by:

$$V = \frac{1}{N_r} \sum_{i=1}^{N_r} x_i^2, \tag{13}$$

where $N_r$ is the number of realizations of $X$. The convergence noise is by definition:

$$Y = V - \sigma_X^2 = \frac{1}{N_r} \sum_{i=1}^{N_r} x_i^2 - \sigma_X^2. \tag{14}$$

It is, in turn, a random variable. Its mean value is:

$$\langle Y \rangle = \frac{1}{N_r} \sum_{i=1}^{N_r} \langle x_i^2 \rangle - \sigma_X^2 = 0. \tag{15}$$

The variance of $Y$ can be written as:

$$
\begin{aligned}
\sigma_Y^2 &= \langle Y^2 \rangle - \langle Y \rangle^2 \tag{16} \\
&= \left\langle \left( \frac{1}{N_r} \sum_{i=1}^{N_r} x_i^2 - \sigma_X^2 \right)^2 \right\rangle \\
&= \left\langle \left( \frac{1}{N_r} \sum_{i=1}^{N_r} x_i^2 \right)^2 \right\rangle + \sigma_X^4 - 2\sigma_X^2 \times \frac{1}{N_r} \sum_{i=1}^{N_r} \langle x_i^2 \rangle \\
&= \left\langle \frac{1}{N_r^2} \sum_{i,j} x_i^2 x_j^2 \right\rangle - \sigma_X^4 \\
&= \left\langle \frac{1}{N_r^2} \sum_{i=1}^{N_r} x_i^4 + \frac{1}{N_r^2} \sum_{i \neq j} x_i^2 x_j^2 \right\rangle - \sigma_X^4 \\
&= \frac{1}{N_r^2} \sum_{i=1}^{N_r} \langle x_i^4 \rangle + \frac{N_r (N_r - 1)}{N_r^2} \sigma_X^4 - \sigma_X^4 \\
&= \frac{3}{N_r} \sigma_X^4 - \frac{1}{N_r} \sigma_X^4 \\
&= \frac{2}{N_r} \sigma_X^4.
\end{aligned}
$$

The variance of the convergence noise $\sigma_Y^2$ can therefore be deduced from the variance of $X$. In practice the latter is unknown, so we approximate $\sigma_X^2$, in the last line of Eq. (16), by its empirical estimate $V$.

### Acknowledgments